Nano Research

Open Access

Research Article

Highly stable spherical metal-organic framework micromotors engineered via topological distortion for photocatalytic uranium extraction

Muhammad Ikram[1,2] ✉, Iltaf Muhammad[3], Yongquan Zhou[1], Israr Masood ul Hasan[4], Hanif Khan[5], and Yongxiang Gao[2] ✉

[1] *Key Laboratory of Green and High-end Utilization of Salt Lake Resources, Qinghai Provincial Key Laboratory of Resources and Chemistry of Salt Lakes, Qinghai Institute of Salt Lakes, Chinese Academy of Sciences, Xining 810008, China*
[2] *Institute for Advanced Study, Shenzhen University, Shenzhen 518060, China*
[3] *School of Mechanical and Electrical Engineering, Hainan Vocational University of Science and Technology, Haikou 571126, China*
[4] *College of Life Science and Technology, Jinan University, Guangzhou 510632, China*
[5] *Department of Radiation Oncology, Penn State Cancer Institute, Hershey, Pennsylvania 17033, USA*

Cite this article: *Nano Research*, **2026**, *19*, 94908602. https://doi.org/10.26599/NR.2026.94908602

ABSTRACT: The integration of metal-organic frameworks (MOFs) into micro- and nanomotors promises advanced functionalities for environmental remediation and active matter research. However, the practical utility of MOF-based motors is constrained by their inherent water instability and the limited exploration of complex collective dynamics. Here, we address these challenges with a novel fluorescent Zn-adeninate-based micromotor (ZABDC) engineered for exceptional aqueous stability. This stability is achieved through a coordination geometry featuring a large Zn-adenine vertex and a short-range linker, which provides steric shielding and enhances the hydrophobicity of the metal-linker bonds. The ZABDC micromotor exhibits a self-propulsion speed of ~ 7 μm·s^{-1} in a low fuel concentration (0.3 wt.% of H_2O_2). This speed is actively enhanced to ~ 15 μm·s^{-1} under visible light illumination. Leveraging this robust platform, we demonstrate two key advances. First, its hierarchical porous structure, rich in nitrogen and oxygen chelating sites, enables highly efficient and selective uranium capture with a capacity of 406 mg·g^{-1} and a distribution coefficient (K_d) of 1.0 × 10^4 mL·g^{-1} in a complex brine matrix. Subsequently, under visible light, adsorbed uranyl ions are photocatalytically precipitated as studtite nanoparticles on the motor surface, achieving effective sequestration. Second, in binary mixtures of active MOFs with passive colloids, they exhibit mimic those of living organisms, such as chasing, escaping, and schooling, mediated by diffusiophoretic interactions driven by self-generated ionic gradients. This work establishes a versatile MOF-based micromotor system, bridging fundamental studies in complex active matter with practical applications in photocatalytic environmental decontamination.

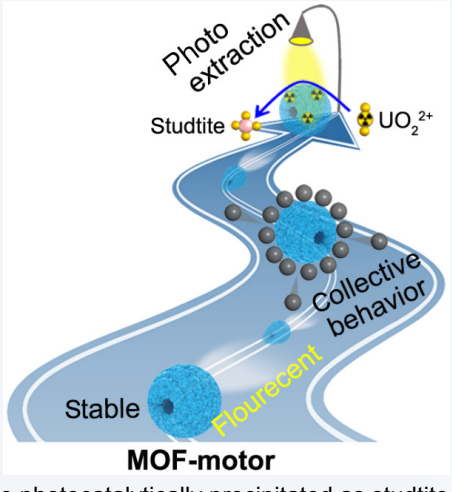

KEYWORDS: metal-organic frameworks (MOF) micromotor, short-range linker, aqueous stability, studtite, uranium capture

1 Introduction

Micro/nanomotors (MNMs) are synthetic micro/nanoscale devices that are broadly categorized by their propulsion mechanism: Chemically powered MNMs harvest energy from local fuel sources, while externally powered MNMs are driven by applied fields, such as magnetic, acoustic, electric, or light [1]. Owing to their unique capabilities, MNMs hold immense potential for advancing fundamental science and enabling a diverse range of applications, including targeted therapeutic interventions and environmental remediation [2–4]. Furthermore, over the past two decades, research on MNMs has yielded profound insights into emergent collective behaviors, which are capable of altering their mechanical

Received: December 17, 2025; **Revised:** January 28, 2026
Accepted: February 24, 2026

✉Address correspondence to Muhammad Ikram, ikram2888@yahoo.com; Yongxiang Gao, yongxiang.gao@szu.edu.cn

properties or morphing in response to external stimuli, leading to distinct biomimetic behaviors, where populations of individual units display coordinated motion and complex organization. In parallel, the field has advanced the development of stimuli-responsive MNMs, which can dynamically alter their mechanical properties or morphology in response to external cues. This synergy between collective intelligence and material adaptation is a hallmark of biological systems, providing a powerful biomimetic platform for studying active matter. Building on this bio-inspired paradigm, MNMs are demonstrating significant potential to revolutionize applications ranging from targeted drug delivery and precision sensing to distributed environmental monitoring and the development of embodied artificial intelligence [5, 6]. A wide variety of collective behaviors has been observed in ensembles of synthetic active MNMs, showcasing phenomena that have no counterparts in equilibrium systems. For instance, Palacci et al. reported the formation of dynamic crystals with giant number fluctuations in photoactive Fe_2O_3-TPM (TPM = 3-trimethoxysilyl propyl methacrylate) colloids [7]. Yang et al. and Lin et al. observed the emergence of ribbon-like structures and swarming behaviors, respectively, in peanut-shaped active hematite colloids [8, 9]. Buttinoni et al. revealed dynamic clustering of SiO_2-carbon Janus colloids in a water-lutidine binary mixture [10]. These investigations primarily focus on unary systems, where all constituents are active. In contrast, Ibele et al. observed schooling behaviors between photosensitive AgCl active particles with passive silica spheres [11]. Similarly, Singh et al. demonstrated tunable self-assembly of TiO_2 Janus colloids with passive SiO_2 spheres under ultraviolet (UV) light illumination [12]. Mou et al. revealed predator–prey behaviors in a binary colloidal system of ZnO and TiO_2 particles in a fuel-free environment, where nonreciprocal attraction and repulsion arose between the particles [5]. These biomimetic systems rely on locally produced chemical gradients as the cue for triggering responses from nearby particles. However, controlling or transitioning between different collective behaviors remains a significant challenge.

Furthermore, MNMs are at the forefront of water purification research, demonstrating exceptional performance due to their high diffusion efficiency, continuous motion, and ability to mix without the need for external mechanical shaking or stirring [13–17]. One of the primary challenges in water purification is the removal of ionic species, particularly uranium and related radionuclides, which pose long-term risks to human health and the environment due to their high mobility, toxicity, and environmental persistence [18, 19]. Additionally, these radionuclides are valuable resources for nuclear energy, which is crucial for producing low-carbon and clean energy. Currently, metal-organic framework (MOF)-based motors have demonstrated excellent performance in wastewater treatment [20], leveraging the MOF tunable chemistry, high porosity, and large surface area for enhanced interactions with target species. Nonetheless, current designs of MOF-micromotors are often hindered by their large dimensions [21], the incorporation of precious metals [17], or their dependency on polymer templates [22], which lead to cumbersome synthesis and reduce the accessible surface area. Thus, it is crucial to develop a simple strategy for synthesizing a sizeable self-propelled micromotor with a low cost, long-term stability, and high adsorption efficiency. In this context, MOFs constructed from carboxylate linkers and metal nodes have been successfully implemented [23, 24]. However, the use of complex and elongated carboxylic acid linkers to maximize MOF porosity introduces several inherent limitations. For instance, longer linkers are often less synthetically accessible, exhibit higher flexibility, and possess lower solubility, complicating their processing. Furthermore, this increased length can weaken the coordination bonds with metal nodes, compromising structural integrity. Consequently, many MOFs constructed with such linkers suffer from hydrolytic instability, leading to breakdown in aqueous environments and sluggish long-term stability, which is detrimental for applications like water remediation. An alternative strategy involves employing large metal vertices in conjunction with shorter organic linkers. This design paradigm simultaneously enhances porosity through the expanded nodes while strengthening the metal-linker bonds via shorter and more rigid connections, ultimately conferring superior stability in aqueous media [25].

Herein, we report a strategy for engineering a fluorescent and spherical vesicle micromotor based on a zinc-adeninate framework (ZABDC). Our design introduces a topological distortion by incorporating a short organic linker (terephthalic acid) instead of a large biphenyl dicarboxylic acid (as used in bio-MOF-100) into the synthesis environment featuring large metal-organic zinc-adeninate vertices. This heuristic strategy extends the lifespan of micromotors in aqueous media, enabling autonomous propulsion through self-diffusiophoresis. We establish the ZABDC micromotors as a highly effective platform for the sequestration of radioactive uranium (UO_2^{2+}) across a range of environmentally relevant conditions. Their excellent performance is attributed to a synergistic combination of a high surface area with hierarchical porosity, sustained autonomous mobility, and excellent aqueous stability. Furthermore, the inherent anionic character of the framework promotes the rapid electrostatic attraction and uniform distribution of UO_2^{2+} cations. This process is augmented by a robust ion-exchange mechanism, which collectively enables superior adsorption capacity and kinetics. Moreover, we investigate the emergent collective behaviors in binary mixtures of active ZABDC micromotors and passive particles, focusing on the impact of surface charges of the particles. We reveal a transition from repulsion behaviors to schooling with negative charge TPM and positive charge polystyrene (PS) as tracer particles, by altering the concentration of peroxide as a fuel. Our work establishes a versatile platform for designing MOF-based micromotors with dual capabilities in emergent collective behavior and environmental remediation. The synthetic strategy, grounded in the modular assembly of metal nodes and organic ligands, provides a blueprint that can be readily adapted to the vast chemical space of MOFs, paving the way for a new generation of tailored active materials.

2 Experimental section

2.1 Synthesis of vesicle Zn-adeninate-MOFs micromotor (ZABDC)

ZABDC micromotors were synthesized via a solvothermal method. Three stock solutions were prepared in N,N-dimethylformamide (DMF): adenine (5 mM), zinc nitrate hexahydrate (5 mM), and 1,4-benzenedicarboxylic acid (terephthalic acid, 10 mM). In a typical synthesis, 5 mL of the adenine solution, 10 mL of the zinc nitrate solution, and 5 mL of the terephthalic acid solution were combined in a glass vial. To this mixture, 5 mL of DMF, 2 mL of ethanol, and 0.5 mL of deionized water were added. The sealed vial was ultrasonicated for 10 min to ensure homogeneity and then heated

statically at 85 °C for 24 h. After cooling to room temperature, the resulting white crystalline product was collected and washed repeatedly with a DMF/ethanol/water mixture (12.5:1:0.25, v/v/v) to remove unreacted precursors and impurities. The final product was dried under an inert atmosphere at 40 °C for 24 h. For comparison, the parent Bio-MOF-100 was synthesized following an identical procedure, but with 4,4'-biphenyldicarboxylic acid replacing 1,4-benzenedicarboxylic acid as the organic linker.

2.2 COMSOL simulation

Simulations were performed using COMSOL Multiphysics software (version 6.3). A coupled analysis of the electric potential and flow fields surrounding a Zn-MOF (ZABDC) particle was conducted by simultaneously solving the electrostatics and creeping flow physics modules. The computational geometry consisted of a two-dimensional fluid domain with a single MOF particle at its center. Within the creeping flow module, the outer boundaries of the domain were set as open at the top and bottom, and as slip conditions at the sides.

In the model, the catalytically active surface of the MOF particle emits ions (H^+ and OH^-) at a constant flux, J. A key step was translating this ionic flux into an electrical driving force. This was achieved by applying an equivalent surface charge density on the particle surface within the electrostatics module, calculated from the difference in flux and diffusion coefficients of the two ion species. This surface charge generates a self-induced electric field.

The electrical boundary condition at the active surface, applicable outside the electrical double layer, is defined by the normal gradient of the electric potential (φ)

$$\frac{\partial \phi}{\partial n} = \frac{J k_B T}{2 e n_0} \left(\frac{1}{D^+} - \frac{1}{D^-} \right) \quad (1)$$

where k_B is the Boltzmann constant, T is the absolute temperature, e is the elementary charge, n_0 is the bulk ion concentration, and D^+ and D^- are the diffusion coefficients of H^+ and OH^-, respectively. For inert surfaces, the no-flux condition corresponds to $\partial\phi/\partial n = 0$. In the bulk fluid, beyond the double layer, the electrostatic potential is governed by Laplace's equation, $\nabla^2\phi = 0$.

The computed electric field was then coupled to the fluid motion via an electroosmotic slip boundary condition on the particle surface in the creeping flow module. Subsequently, the flow field in the low-Reynolds-number regime is described by the Stokes equations

$$\mu \nabla^2 u = \nabla p \quad (2)$$

$$\nabla \cdot u = 0 \quad (3)$$

where u is the fluid velocity, p is the pressure, and μ is the dynamic viscosity of the solution. This coupled approach yielded the steady-state distributions of both electric potential and flow velocity around the particle.

2.3 Characterization

Powder X-ray diffraction (PXRD) was conducted using a Rigaku MiniFlex 600 diffractometer. Morphological and elemental composition were performed using a Thermo FEI Talos F200X transmission electron microscopy (TEM) operated at 200 kV, equipped with an energy-dispersive X-ray (EDX) spectrometer. Scanning electron microscopy (SEM) was conducted on a Hitachi Regulus 8100 microscope at an accelerating voltage of 15 kV. Fourier transform infrared (FTIR) spectroscopy was carried out on a Perkin-Elmer spectrometer at room temperature. Solid-state ^{13}C nuclear magnetic resonance (NMR) spectra were recorded on a Bruker AVANCE 300 MHz spectrometer (40.6 MHz for 13C) using DMSO-D6 as the solvent. Thermogravimetric analysis (TGA) was performed on a Themys instrument under a N_2 atmosphere with a temperature ramp to 1000 °C. X-ray photoelectron spectroscopy (XPS) was conducted on a Thermo Escalab250Xi spectrometer using a monochromatic Al Kα X-ray source ($h\nu$ = 1486.6 eV) with a resolution of 0.45 eV to determine the surface composition and elemental oxidation states. X-ray absorption fine structure (XAFS) measurements were performed at the BL-27B beamline of the Photon Factory (PF) in Tsukuba, and the data were processed using the Athena software. The specific surface area and porosity were determined from nitrogen adsorption–desorption isotherms measured at 77 K using a Micromeritics TristarII3020 analyzer; the surface area was calculated by the Brunauer–Emmett–Teller (BET) method, and pore size distribution was derived from the Barrett–Joyner–Halenda (BJH) model. Mott–Schottky (MS) analysis was performed using a CHI660C electrochemical workstation. Ultraviolet–visible diffuse reflectance spectra (UV–vis DRS) were acquired on a Shimadzu UV-2550 spectrometer. Zeta potential measurements were carried out using a NanoBrook 90PlusPALS zeta potential analyzer. Optical microscopy images were captured using an Olympus IX73 inverted microscope equipped with a 60× oil-immersion objective (numerical aperture (NA) = 1.42), a Ximea xiQ digital camera, and a CoolLED PE-300 ultra light source. Photocurrent response was measured on a CHI360E electrochemical workstation under illumination from a 300 W Xenon lamp (320 nm ≤ λ ≤ 780 nm). Metal ion concentrations in solution were quantified by inductively coupled plasma mass spectrometry (ICP-MS, Agilent 7700 series) and inductively coupled plasma optical emission spectrometry (ICP-OES, PerkinElmer Avio 220).

3 Results and discussion

3.1 Preparation and characterization of ZABDC micromotor

Bio-MOF-100 is selected as the scaffold MOF due to its mesoporous structure, which is composed of metal-adeninate building blocks interconnected with biphenyl dicarboxylate (BPDC) linkers. These components are periodically arranged to form a three-dimensional polyhedron framework (Fig. S1 in the Electronic Supplementary Material (ESM)) [26]. Spherical ZABDC vesicle colloids were synthesized by employing a short organic linker, 1,4-benzene dicarboxylic acid (BDC), in place of the long and rigid BPDC, in combination with large Zn-adeninate vertices in a DMF solution. This strategic substitution of the linker enhances steric protection and increases the hydrophobicity of the metal–linker bonds, thereby improving the aqueous stability of the MOFs [25]. The crystal structure of ZABDC consists of discrete zinc-adeninate secondary building units (SBUs), each comprising four adeninate ligands coordinated to eight zinc cations, interconnected by BDC linkers (Fig. 1(a) and Fig. S2 in the ESM). This connectivity propagates in three dimensions, adopting an augmented LCS (a-LCs) topology that generates a framework with large and accessible cavities along the [110], [101], and [011] directions (Fig. 1(a)) [27]. Following synthesis and aging at 85 °C

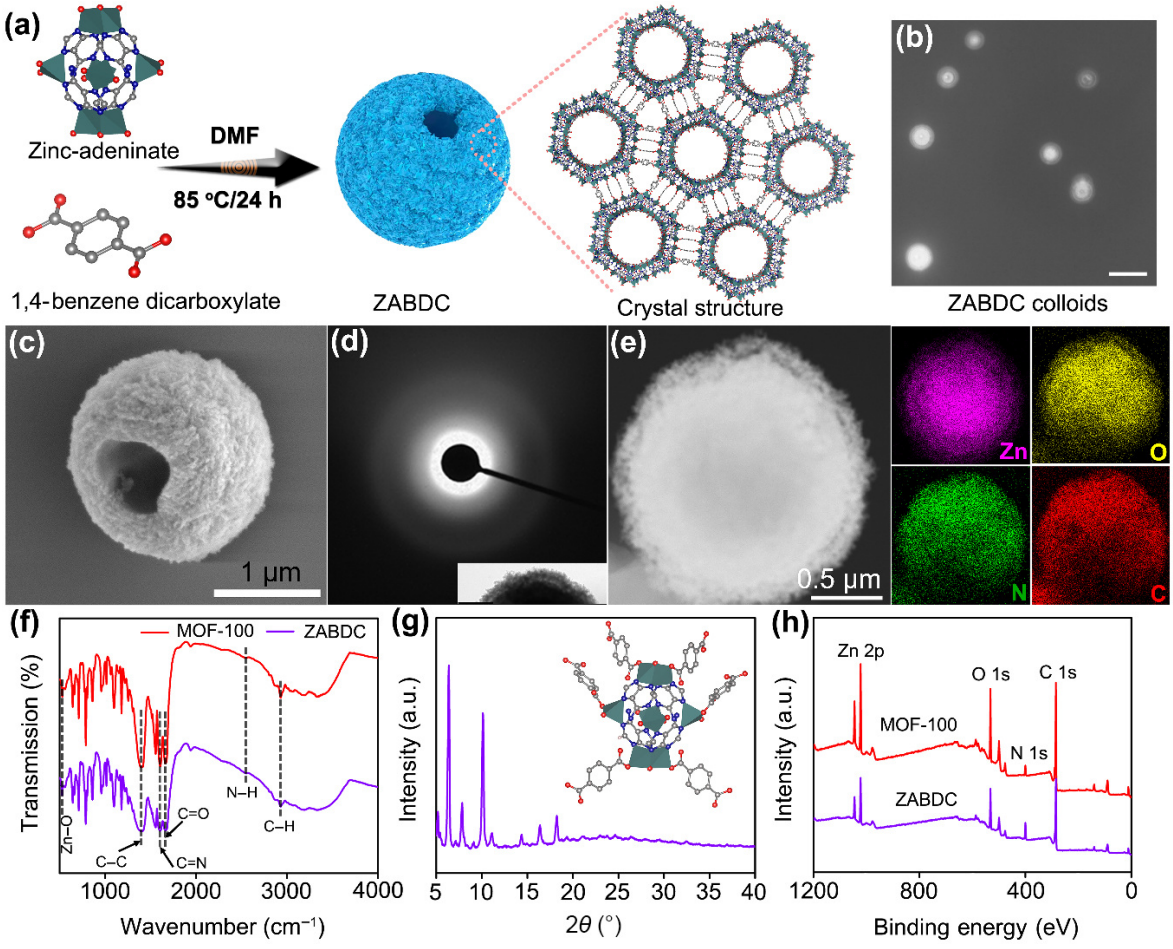

Figure 1 (a) Schematic of the growth process of the ZABDC and unit structure, composed of zinc adeninate vertices linked by BDC ligands, with a perspective view of the (111) crystal facet. (b) Optical image of the suspended ZABDC colloids in water, showing fluorescence under blue light exposure (scale bar is 5 μm). ((c) and (d)) SEM and SAED patern. (e) Bright field TEM and EDX mapping of the ZABDC colloids. (f) Comparative FTIR spectra. (g) XRD pattern of ZABDC, with the inset showing the unit structure, composed of Zn vertices (zinc adeninate) combined with organic building blocks (1,4-benzene dicarboxylic acid). (h) Comparative XPS survy spectra of MOF-100 and ZABDC.

for 24 h, spherical vesicle-like ZABDC MOF colloids with a spongy hierarchical surface were obtained, with an average size of ~ 2 μm (Figs. 1(b) and 1(c)), which was further confirmed by TEM (Fig. S3 in the ESM). The as-prepared colloids were suspended in deionized (DI) water and observed under fluorescence microscopy, revealing fluorescence intensity comparable to the parental bio-MOF-100 upon light excitation (Fig. 1(b) and Fig. S1 in the ESM). The rapid instability of Bio-MOF-100 in aqueous media is visually demonstrated in Fig. S4 in the ESM, which shows immediate surface degradation upon contact with water. This phenomenon is attributed to the quick collapse of coordination bonds between the metal nodes and organic linkers.

In contrast, ZABDC micromotors maintained their structure and morphology even in acidic media, which was confirmed by SEM and XRD (Fig. S5 in the ESM). Thermogravimetric analysis (TGA) demonstrates the thermal stability of the ZABDC framework up to 400 °C (Fig. S6 in the ESM). The profile reveals a multi-stage decomposition process. An initial weight loss of 18% at 179 °C is attributed to the evolution of adsorbed water and residual solvent molecules. A subsequent 10% loss at approximately 260 °C corresponds to the removal of guest molecules, such as DMF, from the porous structure. The primary decomposition event is marked by a pronounced endothermic peak at 508 °C, resulting in a total weight loss of 59%, which signifies the collapse of the organic framework. The remaining 41% mass is consistent with a stable carbonaceous residue. The selected area electron diffraction (SAED) pattern of the ZABDC MOF lacks discernible diffraction rings or spots attributed to the known electron-beam sensitivity (Fig. 1(d)). Elemental mapping reveals a homogenous distribution of Zn, O, N, and C throughout sphere architectures, with EDX spectroscopy quantifying their respective atomic proportions (Fig. 1(e) and Fig. S7 in the ESM). These results demonstrate the successful formation of the ZABDC framework through coordination of Zn metals with adenine and 1,4-benzene dicarboxylic acid organic linkers.

FTIR spectroscopy confirmed the successful synthesis of ZABDC spheres, with the spectrum exhibiting characteristic peaks analogous to the parent Bio-MOF-100 framework (Fig. 1(f)). The presence of a low-intensity peak at 530 cm^{-1} is attributed to Zn–O stretching vibrations, confirming the coordination of zinc ions with the organic linkers. Distinct bands at 1606 and 1663 cm^{-1} correspond to the stretching modes of C=N and C=O bonds, respectively. A broad peak observed at 1398 cm^{-1} is assigned to C–C stretching vibrations, while the weak bands at 2547 and 2933 cm^{-1} are consistent with N–H and C–H vibrations, respectively [26, 28, 29]. PXRD analysis further confirms the phase purity of the ZABDC MOF. The diffraction pattern exhibits close alignment

with the simulated spectrum of Bio-MOF-100, indicating an isoreticular framework (Fig. 1(g)). The observed shift of the reflections to higher 2θ angles is consistent with a contraction of the unit cell, a direct consequence of incorporating the shorter terephthalic acid linker compared to the longer BPDC linker used in the parent structure [30]. Comparative XPS survey spectra of bio-MOF-100 and ZABDC confirm the presence of Zn, O, C, and N on the surface of the MOF materials (Fig. 1(h)).

The Zn 2p spectra for both materials exhibit characteristic peaks at 1022.2 (Zn $2p_{3/2}$) and 1045.3 eV (Zn $2p_{1/2}$), consistent with Zn(II) oxidation in a coordination environment (Fig. 2(a)). Deconvolution of the O 1s spectra reveals three peaks at 531.4, 532.1, and 532.8 eV, assigned to Zn–O, C=O, and C–O bonds, respectively (Fig. 2(b)). The N 1s spectra are deconvoluted into two peaks at 399.7 and 400.5 eV, the peak at 399.7 eV is assigned to the coordination of the Zn metal ion with the N of adenine by electron pair sharing, and the peak at 400.5 eV is attributed to N–C bonding (Fig. 2(c)). Similarly, the C 1s spectra split into three distinct peaks, C–C (284.6 ± 2 eV), C–O (285.3 ± 2 eV), and C=O (288.6 ± 2 eV) (Fig. 2(d)). A notable shift to higher binding energies is observed in the C 1s and N 1s spectra of ZABDC compared to Bio-MOF-100, which is attributed to the altered electron-withdrawing characteristics and coordination geometry induced by the shorter organic linker [28, 31].

XAFS spectroscopy was employed to probe the valence state and local coordination environment of Zn atoms within the ZABDC framework. The absorption edge energy of ZABDC in the X-ray absorption near-edge structure (XANES) spectra lies far from Zn foil, but close to Zn-acetate or ZnO references, indicating the divalent oxidation for Zn (Fig. 2(e)) [32]. Furthermore, the spectral line shape and intensity closely resemble those of Zn-acetate, suggesting a similar oxygen-dominated first coordination shell. The Fourier-transformed k^2-weighted extended X-ray absorption fine structure (FT-EXAFS) without phase correction further elucidated the local coordination environment of Zn in ZABDC. The absence of the Zn–Zn scattering at 2.33 Å in ZnO, Zn-acetate, and ZABDC suggests the atomic dispersion of Zn (Fig. 2(f)). Instead, ZABDC exhibits a prominent first coordination shell peak at ~ 1.56 Å, which is slightly shorter than the characteristic Zn–O bond length observed in both ZnO and Zn-acetate (~ 1.59 Å). The observed contraction is consistent with the formation of Zn–N bonds in addition to Zn–O bonds, as the backscattering from the lighter nitrogen atoms in the adenine linker leads to a shorter apparent distance in the FT-EXAFS spectrum [33]. The corresponding

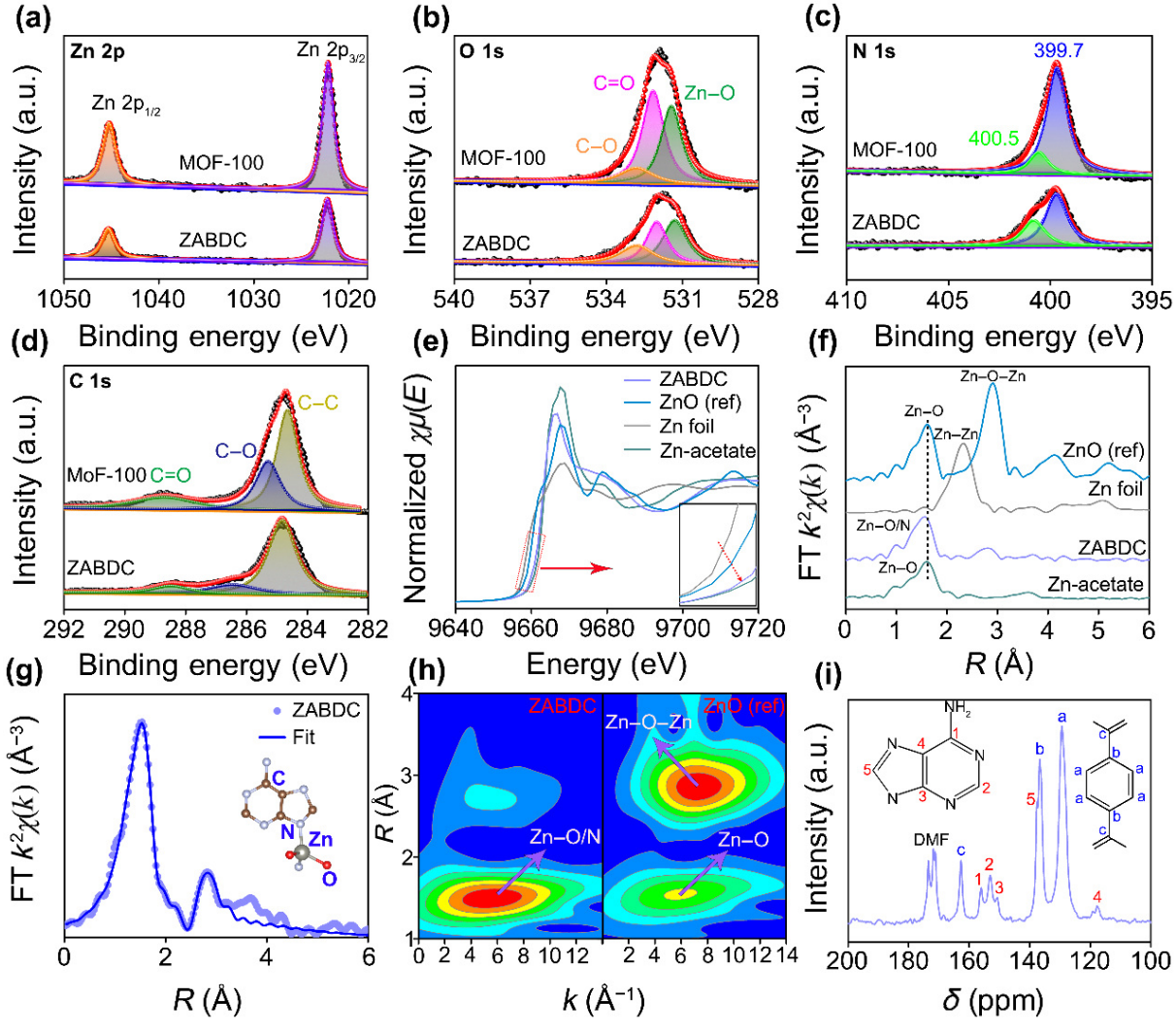

Figure 2 ((a)–(d)) High-resolution spectra of (a) Zn, (b) O 1s, (c) N 1s, and (d) C 1s of ZABDC. (e) Zn K-edge XANES and (f) FT-EXAFS spectra of ZABDC, ZnO, Zn foil, and Zn-acetate. (g) EXAFS fitting of ZABDC in *R* space. (h) WT-EXAFS plots of ZABDC and ZnO. (i) ^{13}C solid state NMR spectra of the ZABDC MOF spheres.

EXAFS fitting results for ZABDC, ZnO, and zinc-acetate in *R* and *k* spaces are presented in Fig. 2(g), and Figs. S8 and S9 and Table S1 in the ESM. The excellent agreement between the experimental data and the theoretical fit strongly supports a first-shell coordination environment of Zn with two nitrogen and two oxygen atoms (Zn-N_2/O_2). Quantitative analysis yields a coordination number of 4 for the Zn–O/N bonds at an average bond distance of 2.03 Å, which is consistent with previously reported structures and confirms the proposed coordination geometry [32, 34, 35]. Wavelet transform (WT) analysis of the EXAFS spectra provides enhanced resolution of the local coordination environments in ZABDC and the ZnO reference across both *R* and *k* spaces (Fig. 2(h)). The intensity maximum for ZABDC is observed at 5.3 $Å^{-1}$ in *k* space and at 1.47 Å in *R* space, which does not coincide with the Zn–O path in ZnO (5.5 $Å^{-1}$ in *k* space and 1.53 Å in *R* space), suggesting the contribution of N in the ZABDC framework to form Zn–N/O coordinations. Furthermore, a weak signal corresponding to the Zn–O–Zn scattering path was observed in ZABDC, which is prominent in the ZnO reference. This provides additional and direct evidence for the atomic dispersion of Zn within the ZABDC framework [32, 36]. ^{13}C NMR analysis was further conducted to investigate the organic ligands within the ZABDC framework (Fig. 2(i)). The spectrum confirms the presence of both adenine and benzene carboxylate organic linkers. The signals at 129.4, 136.7, and 162.7 ppm are assigned to the aromatic-a, quaternary aromatic-b, and carbonyl-c carbons of the carboxylate linker, respectively, consistent with Ref. [37]. Furthermore, the five distinct carbons of the adenine ligand are clearly resolved; the peaks at 157.0, 153.0, 150.7, 137.5 (shoulder), and 117.7 ppm correspond to positions 1, 2, 3, 4, and 5 within its bicyclic ring structure, respectively [38, 39].

3.2 Self-propulsion of the ZABDC micromotor and mechanism

The self-propulsion of ZABDC micromotors was characterized in DI water and H_2O_2 solutions under both dark and illuminated conditions (Fig. S10 and Videos S1 and S2 in the ESM). In DI water, the micromotors exhibited only Brownian motion. Visible light illumination alone induced autonomous propulsion (7 ± 0.3 μm·s^{-1}), accompanied by strong fluorescence from the structure π-conjugated aromatic ligands [40, 41]. With 0.3 wt.% of H_2O_2 fuel in the dark, self-propulsion reached 6.8 ± 0.2 μm·s^{-1}. Upon illumination, the speed increased synergistically to 15.0 ± 1 μm·s^{-1}, demonstrating high photoresponsivity (Fig. 3(a)). The self-propulsion of ZABDC micromotors is driven by catalytic H_2O_2

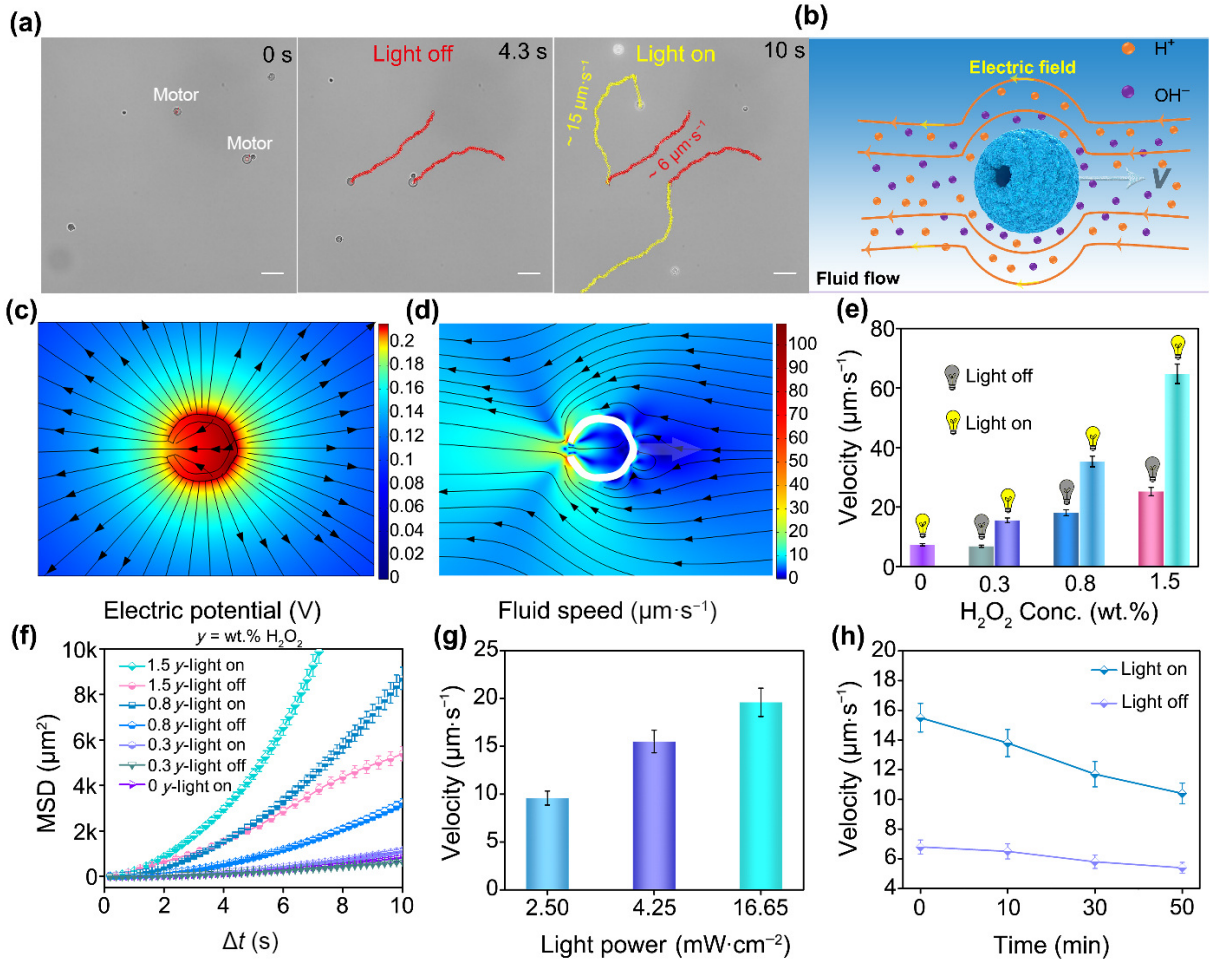

Figure 3 Self-propulsion of ZABDC micromotors. (a) Time-lapsed trajectories display the self-propulsion of the micromotor in DI water in 0.3 wt.% of H_2O_2 as fuel in the absence and presence of external light (scale bar is 8 μm). (b) Schematic representation of the self-propulsion mechanism of the micromotor. ((c) and (d)) Electrical potential distribution (color-code) and flow field of ZABDC micromotor driven by H_2O_2, simulated by COMSOL, a multi-physics field finite element analysis software. ((e) and (f)) Speed of ZABDC micromotors and corresponding MSD in different concentrations of H_2O_2 in on/off visible light. (g) Speed of micromotor in different light intensity in the presence of 0.3 wt.% of H_2O_2. (h) Self-propulsion stability of the ZABDC in the presence and absence of external light in 0.3 wt.% of H_2O_2.

decomposition, enhanced under visible light. In the dark, a Fenton-like reaction at ZABDC active sites initiates motion (Eq. (4)).

$$\mathrm{ZABDC} + 2\mathrm{H_2O_2} \rightarrow 2\mathrm{H^+} + 2\mathrm{OH^-} \quad (4)$$

Under illumination, the photogenerated charge carriers (Eq. (5)) further catalyze H_2O_2 decomposition via multiple pathways (Eqs. (6)–(8)), intensifying the production of H^+ and OH^- ions.

$$\mathrm{ZABDC} \xrightarrow{h\nu} \mathrm{e^-} + \mathrm{h^+} \quad (5)$$

$$\mathrm{H_2O_2} \rightarrow \mathrm{O_2} + 2\mathrm{H^+} + 2\mathrm{e^-} \quad (6)$$

$$\mathrm{O_2} + \mathrm{e^-} \rightarrow {}^{\bullet}\mathrm{O_2^-} \quad (7)$$

$$\mathrm{H_2O_2} + \mathrm{e^-} \rightarrow {}^{\bullet}\mathrm{OH} + \mathrm{OH^-} \quad (8)$$

The resulting ionic gradients, with their markedly different diffusion coefficients (D_{OH^-} = 5.273 × 10^{-5} $cm^2 \cdot s^{-1}$; D_{H^+} = 9.31 × 10^{-9} $cm^2 \cdot s^{-1}$), propel the micromotor via self-diffusiophoresis [42, 43]. The faster-diffusing H^+ generates a local electric field that acts on the particle's surface (Fig. 3(b)), while the intrinsic cavity provides necessary asymmetry. Finite element analysis (COMSOL; details in Fig. S11 in the ESM) validates this mechanism. The model confirms that catalytic ion generation creates an outward flux. The diffusion disparity spontaneously forms an electric field (Fig. 3(c)), which the cavity distorts to induce an electroosmotic flow along the inner wall. This flow propels the micromotor forward, away from its opening (Fig. 3(d)), qualitatively confirming ionic diffusiophoresis as the propulsion mechanism. ZABDC micromotor speed increased with H_2O_2 concentration and light intensity. Speed rose from 18 (dark) to 35 μm·s^{-1} (2.50 mW·cm^{-2} blue light) at 0.8 wt.% of H_2O_2, and from 25 to 64 μm·s^{-1} at 1.5 wt.% (Figs. 3(e) and 3(f), and Video S2 in the ESM). At 0.3 wt.% of H_2O_2, the speed increased with light intensity from 7 (2.50 mW·cm^{-2}) to 20 μm·s^{-1} (16.65 mW·cm^{-2}) (Fig. 3(g)). The Autonomous motion sustained for more than 50 min, demonstrating effective durability (Fig. 3(h) and Video S3 in the ESM).

3.3 Collective behaviors of the ZABDC micromotor

To probe how ionic gradients from ZABDC micromotors influence their local environment, we employed charged tracer particles of TPM (ζ = −33 mV) and PS (ζ = +35 mV) (Fig. S12 in the ESM). Figure 4(a) schematizes this binary active-passive system, where the interactions are mediated by chemical ingredients from surface catalysis. The collective behavior is tunable by H_2O_2 concentration, while light illumination does not change the fundamental interaction nature; it only enhances the surface reaction rate, amplifying the effects. At a low H_2O_2 concentration (0.3 wt.%), the repulsive interactions with negatively charged TPM particles induce predator–prey-like dynamics; the active micromotors chase passive TPM particles, which exhibit evasive motion (Fig. 4(b) and Video S4 in the ESM). The predator micromotors sense environmental cues, dynamically adjusting their velocity and direction to achieve pursuit speeds up to 17 μm·s^{-1}, a behavior reflected in their characteristic mean squared displacement (MSD) curves (Fig. S13 in the ESM). In contrast, with positively charged PS particles, the system exhibits cohesive schooling behavior, forming collectively moving clusters that accumulate more passive particles over time (Fig. 4(d) and Video S5 in the ESM). These distinct cargo manipulation capabilities arise from the catalytic decomposition of H_2O_2, which generates gradients of H^+ and OH^- ions. Their differing diffusion coefficients spontaneously create a local electric field (E) directed toward the negatively charged ZABDC. This field then acts via electrophoresis, repelling the TPM particles and attracting the PS particles, thereby enabling selective particle transport. To explore interparticle communication, we increased the H_2O_2 concentration to 2.0 wt.%. At this elevated fuel level, the interactions reversed, and the active ZABDC particle began attracting neighboring negative TPM colloids, initiating competitive attachment (Fig. 4(c) and Video S4 in the ESM). This led to the dynamic self-organization of a stable and single-layered shell of passive particles ($N \approx 10$) around the motor, maintained in dynamic equilibrium. Conversely, with positively charged PS particles, the active ZABDC strongly repelled them, creating a large exclusion zone (~ 50 μm) (Fig. 4(e) and Video S5 in the ESM). Any initially adhered PS particles via electrostatic interactions were pumped away upon light exposure due to enhanced ion release. These behavioral transitions are governed by electrokinetics from fuel decomposition. At high H_2O_2 concentrations, the catalytic reaction releases Zn^{2+} ions (confirmed by ICP-MS). Due to its low diffusion coefficient ($D_{Zn^{2+}}$ = 0.703 × 10^{-5} $cm^2 \cdot s^{-1}$), Zn^{2+} accumulates around the particle, generating a transient electric field directed away from the surface [42, 44]. This field attracts negative TPM particles inward via electrophoresis while driving positive PS particles outward, creating the observed exclusion zone.

3.4 Uranium extraction by ZABDC micromotors

MOFs are highly desirable porous adsorbents, renowned for their exceptional capacity to capture uranium ions from aqueous solutions [45, 46]. Conventionally, maximizing the adsorption kinetics and capacity of MOF-based adsorbents requires vigorous mechanical stirring or shaking. Here, we present self-propelled ZABDC micromotors with a high surface area (1327 $m^2 \cdot g^{-1}$) and optimal porosity (Fig. S14 in the ESM), which achieve superior uranium adsorption efficiency through autonomous motion without the need for external agitation. The superior uranium adsorption capacity of the ZABDC micromotors is attributed to a synergistic combination of their intrinsic material properties and autonomous mobility, with excellent photocatalytic activity toward uranyl. The hierarchical morphology and large surface area provide numerous binding sites that facilitate a pore-filling effect and multiple channels for pollutant capture (Figs. 5(a) and 5(b)). Furthermore, the anionic framework of the ZABDC matrix (or motor body) strongly attracts uranium cations, enabling their rapid sequestration into the internal pores. These pores are rich in dimethylammonium ($Me_2NH_2^+$) cations, which further enhance uranium uptake through an efficient ion-exchange mechanism (Fig. 5(c)) [26].

Adsorption kinetics were investigated at an initial uranium concentration of 11.6 mg·L^{-1} using an adsorbent dosage of 1000 mg·L^{-1} at neutral pH. The self-propulsion of the ZABDC micromotors in uranium-contaminated water was confirmed both with and without external light irradiation in 0.5 wt.% of H_2O_2 (Fig. 5(a) and Video S6 in the ESM). The most remarkable performance was observed under light illumination. ZABDC-C (light, no fuel) and ZABDC-D (light with 0.5 wt.% of H_2O_2) exhibited rapid adsorption kinetics, reducing the uranium concentration from 11.6 to 0.65 and 0.08 mg·L^{-1}, corresponding to removal efficiencies of 94% and 99% within 70 min, respectively, (Figs. 5(d) and 5(e), and Eq. (S1) in the ESM). In contrast, the

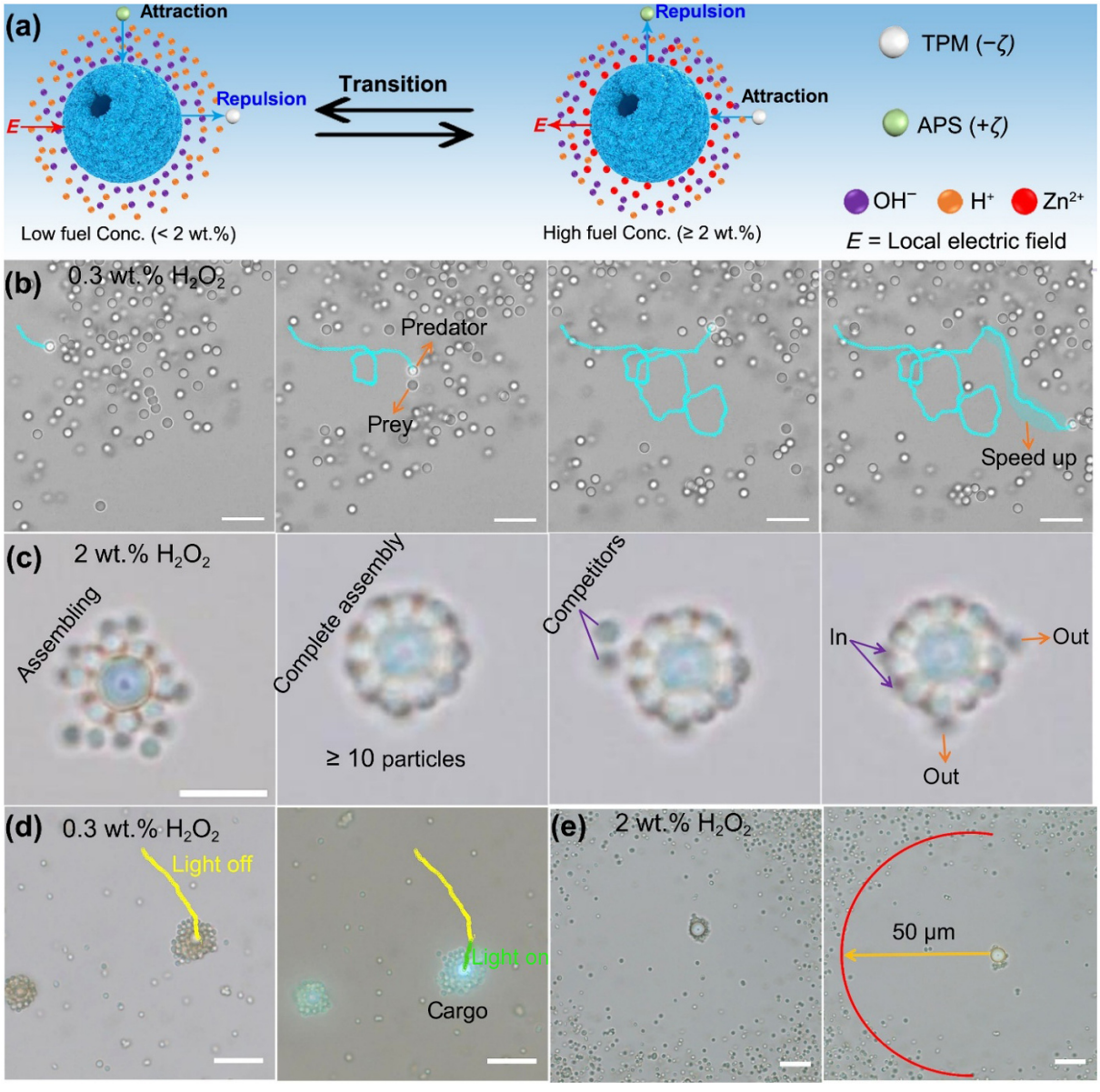

Figure 4 (a) Schematic showing the transition in collective behavior of the ZABDC micromotor with tracer colloids in different H_2O_2 concentrations. (b) Predator-prey behaviors between active ZABDC micromotor and passive TPM(−) particles in the presence of 0.3 wt.% of H_2O_2 (scale bar is 10 μm). (c) Sequence of the optical images showing the raft of the passive TPM particles around the ZABDC micromotor in the presence of 2 wt.% of H_2O_2 (scale bar is 5 μm). ((d) and (e)) Optical images showing attraction between the active micromotor and passive PS(+) particles, along with cargo delivery in the presence of 0.3 wt.% of H_2O_2, and exclusion between the ZABDC and PS particles in 2 wt.% of H_2O_2 (scale bar is 10 μm).

removal efficiencies for ZABDC-A (dark, no fuel) and ZABDC-B (dark with 0.5 wt.% of H_2O_2) were significantly lower, reaching only 56% and 68%, respectively. The enhanced removal kinetics for ZABDC-D and ZABDC-C under visible light (300 W xenon lamp, $\lambda \geq 420$ nm) are attributed to a synergistic combination of photocatalytic activity and enhanced self-propulsion. All kinetic data were well matched with the pseudo-second-order model, showing a correlation coefficient of ≥ 0.99 for all conditions (Fig. S15, Table S2, and Eq. (S3) in the ESM), suggesting that chemisorption is the dominant adsorption mechanism [47]. It is worth noting that the fast adsorption rate of ZABDC-D stands in stark contrast to conventional uranium adsorbents, which typically require hours to days to reach saturation [48, 49]. The maximum adsorption capacity of ZABDC-A, ZABDC-B, ZABDC-C, and ZABDC-D reached ~ 81, ~ 198, ~ 351, and ~ 406 $mg \cdot g^{-1}$, respectively (Fig. 5(f), and Table S3 and Eq. (S2) in the ESM). The equilibrium adsorption data for all systems showed an excellent fit to the Langmuir isotherm model, as evidenced by high correlation coefficients (R^2) indicating monolayer adsorption. The maximum adsorption capacity for ZABDC-D, derived from the model, was 406.8 $mg \cdot g^{-1}$, in agreement with experimental findings. Furthermore, ZABDC-D possessed the largest Langmuir constant (K_L = 0.128 $L \cdot mg^{-1}$), consistent with its enhanced adsorption affinity (Table S4 and Eq. (S4) in the ESM). Furthermore, the leaching concentration of Zn^{2+} ions during the entire adsorption process was measured at only 0.41 $mg \cdot L^{-1}$ by ICP-MS, which is well below the threshold value of 4 $mg \cdot L^{-1}$ for drinking water recommended by the World Health Organization (WHO) [50], indicating that the

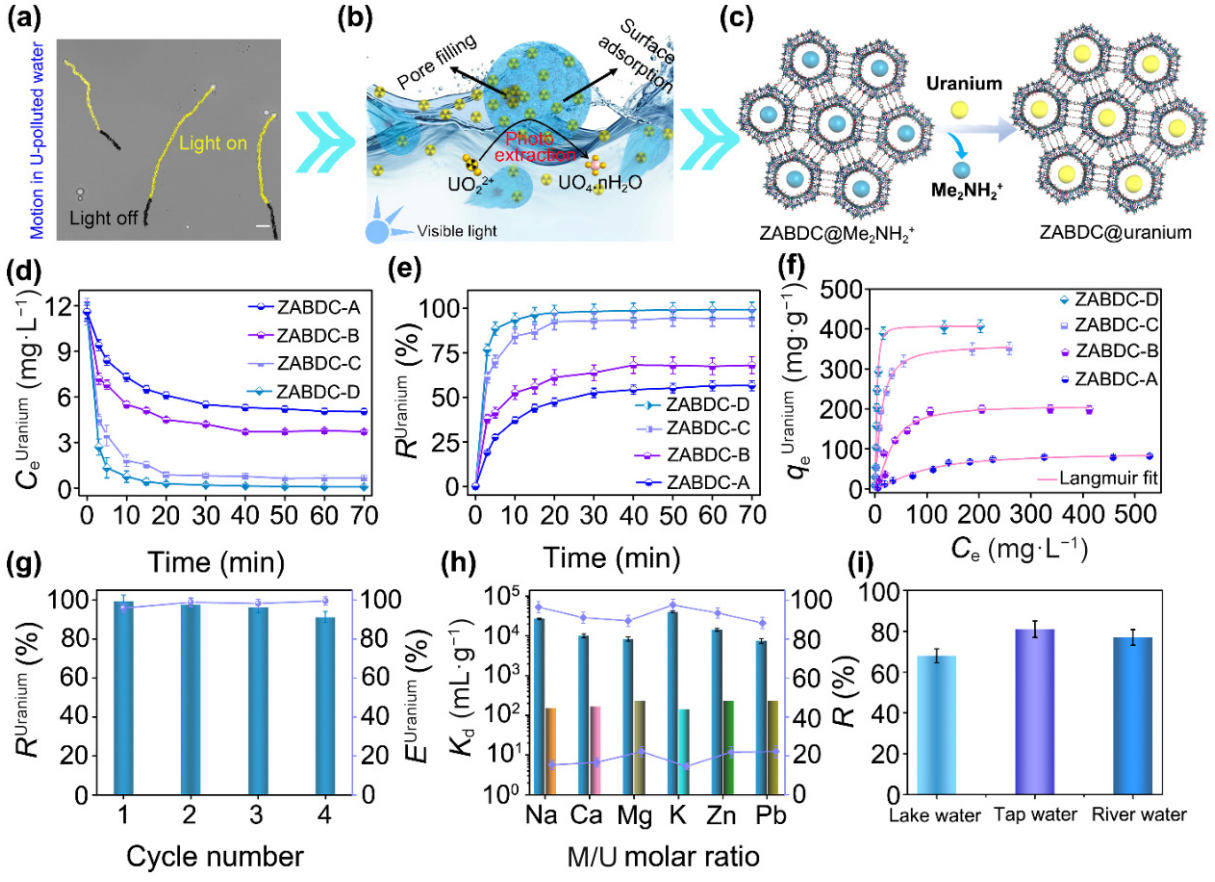

Figure 5 Enhanced uranium removal by a photocatalytic self-propelled ZABDC micromotor. (a) Time-lapsed trajectories display the self-propulsion of the ZABDC micromotors in uranium-contaminated water in 0.5 wt.% of H_2O_2 as fuel in off/up light. ((b) and (c)) Schematic illustrating the pollutant removal mechanism. ((d) and (e)) Adsorption kinetics of uranium (initial concentration, C_0 = 11.6 mg·L^{-1}) under different conditions: ZABDC-A (dark, no fuel), ZABDC-B (dark, with H_2O_2), ZABDC-C (light, no fuel), and ZABDC-D (light, with H_2O_2). (e) Adsorption isotherms at corresponding conditions. (g) Recycling performance of the ZABDC-D micromotors. (h) Selectivity of ZABDC-D micromotors in the presence of interfering metal ions. (i) Uranium removal (R%) of ZABDC in UO_2^{2+} contained lake water (Gas Hure, Qinghai; C_0 = 7.6 mg·L^{-1}), tap water (Xining, Qinghai; C_0 = 10.3 mg·L^{-1}), and river water (Huangshui river, Xining, Qinghai; C_0 = 9.5 mg·L^{-1}).

ZABDC micromotors are safe for use in water treatment applications.

The reusability of the ZABDC-D micromotors was evaluated over four consecutive adsorption–desorption cycles. After each photocatalytic adsorption step, the micromotors were regenerated by ultrasonication in 0.05 M Na_2CO_3 solution, followed by thorough washing with water and DMF. Remarkably, the adsorption efficiency decreased by only 8% after the fourth cycle, while the elution rate (E%) remained consistently high (95%–99%) throughout, demonstrating exceptional recyclability and stable adsorption–desorption performance (Fig. 5(g) and Eq. (S5) in the ESM). The selectivity of the ZABDC-D micromotors for uranium was evaluated in the presence of competing metal ions under visible light illumination. Notably, the distribution coefficient (K_d) for UO_2^{2+} reached a high value of 1.0 × 10^4 mL·g^{-1} with a removal efficiency exceeding 90%, even in solutions containing high concentrations of Na^+, Ca^{2+}, K^+, and Zn^{2+}. In the presence of Mg^{2+} and Pb^{2+}, the K_d value remained substantial at 1.0 × 10^3 mL·g^{-1}, corresponding to removal efficiencies of 89.4% and 88.2%, respectively (Fig. 5(h), and Table S5 and Eq. (S5) in the ESM). These results demonstrate a strong preferential adsorption of uranium over common interfering cations under visible light illumination. This high selectivity arises from synergistic factors, such as the strong affinity between UO_2^{2+} and the active sites, which comprise an uncoordinated carboxylic oxygen and an amine group within the adeninate ligand. Similarly, the ionic radii of the competing ions are less compatible with the optimal coordination geometry of these specific binding sites [14, 51]. Furthermore, the superior photoextraction capability of surface-adsorbed uranyl ions compared to other metal ions under visible light provides an additional selectivity mechanism, effectively locking in the target species. The selectivity of the ZABDC adsorbent under visible light was further evaluated using simulated real water samples (Fig. 5(i)). Despite high concentrations of competing ions (Na^+, Ca^{2+}, Mg^{2+}, and K^+), ZABDC efficiently and selectively extracted uranium from water collected from the Gas Hure Salt Lake (Qinghai, China), achieving a removal efficiency of 68% (C_0 = 7.6 mg·L^{-1}). Removal rates from tap water (C_0 = 10.3 mg·L^{-1}) and river water (C_0 = 9.5 mg·L^{-1}) reached 81% and 77%, respectively. These results confirm that ZABDC retains high adsorption capacity and selectivity for UO_2^{2+} even in complex aqueous matrices.

The adsorption performance of ZABDC-D micromotors was evaluated across a pH range of 3–9 to assess their suitability for acidic nuclear wastewater (Fig. S16 in the ESM). The micromotors demonstrated robust performance over a wide pH range (5–8), achieving a maximum uranium removal efficiency of greater than 99% and a K_d of 1 × 10^5 mL·g^{-1}. Even under more acidic conditions (pH 3–4), significant adsorption was maintained (55%–77%)

with a consistently high K_d value. A slight efficiency reduction to 89% was observed at pH 9, yet the K_d value remained substantial (8×10^3 mL·g^{-1}). The overall adsorption capacity of ZABDC micromotors is competitive with other reported adsorbents for uranium removal (Table S6 in the ESM).

3.5 Optoelectronic properties of ZABDC and interactions with UO_2^{2+}

The strong interaction between UO_2^{2+} ions and the nitrogen/oxygen active sites within the ZABDC framework was confirmed by density functional theory (DFT) calculations in conjunction with physical characterization. Figure 6(a) presents the optimized adsorption configurations of ZABDC with UO_2^{2+}. In the first structure, UO_2^{2+} coordinates directly to the amine group of an adenine linker with a bond distance of 2.35 Å and a nearby nitrogen atom in the six-membered ring with a bond distance of 2.43 Å. This configuration yields an adsorption energy of −4.12 eV, indicating a strong and spontaneous affinity. The second optimized structure reveals that UO_2^{2+} coordinates with a carbonyl oxygen from a carboxylate linker at a shorter bond distance of 2.31 Å, while also binding to a second nitrogen atom in the adenine ring (U–N = 2.46 Å). This configuration, with an adsorption energy of −3.96 eV, also demonstrates robust coordination. The high adsorption energies indicate that ZABDC effectively preconcentrates uranyl ions at the catalyst surface. The charge density difference further corroborates these interactions, showing significant electron accumulation (yellow) around the UO_2^{2+} ion (Fig. 6(b)).

The interaction between UO_2^{2+} and the ZABDC framework was further elucidated for both conditions, ZABDC-C (light, without external H_2O_2) and ZABDC-D (light, with external H_2O_2), using multi-technique characterizations. FTIR analysis revealed a distinct new peak at 916 ± 0.1 cm^{-1} following the photoextraction process in

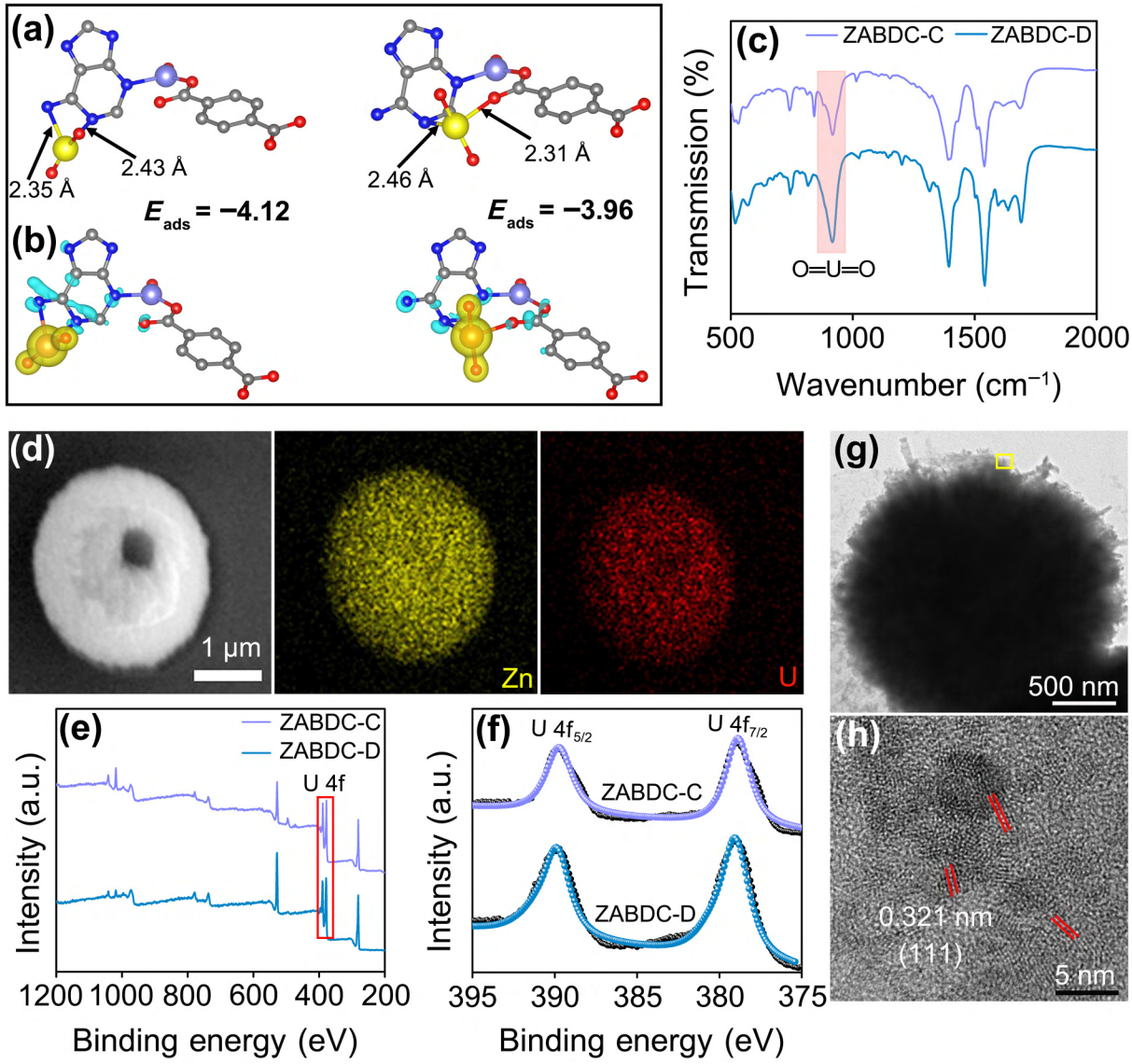

Figure 6 (a) The optimized ZABDC partial structures coordinated with UO_2^{2+} at different sites. (b) Charge density difference, $\Delta\rho = \rho(\text{ZABDC}/[UO_2]^{2+}) - \rho(\text{ZABDC}) - \rho([UO_2]^{2+})$, for UO_2^{2+} adsorption on ZABDC. (c) FTIR spectra of ZABDC-C (light, without external H_2O_2) and ZABDC-D (light, with external H_2O_2) after uranium photoextraction. (d) Bright field SEM and mapping images of ZABDC-D after uranium treatment. (e) XPS survey spectra of ZABDC-C and ZABDC-D after uranium photoextraction. (f) High resolution U 4f spectra of ZABDC-C and ZABDC-D after uranium treatments. ((g) and (h)) TEM and HRTEM images of ZABDC-D after photoextraction of uranium.

both samples (Fig. 6(c)). This peak corresponds to the asymmetric stretching vibration (ν_3) of the uranyl ion, and its appearance confirms the successful coordination of UO_2^{2+} to the active sites within the ZABDC framework [52, 53]. Bright-field SEM and elemental mapping of ZABDC-D demonstrated the structural integrity of the micromotors and a uniform distribution of uranium after treatment (Fig. 6(d)). XPS survey spectra confirmed successful uranium uptake on both ZABDC-C and ZABDC-D (Fig. 6(e)). The U 4f core-level spectrum exhibited characteristic doublets at 379.1 ± 0.1 (U $4f_{7/2}$) and 389.9 ± 0.1 eV (U $4f_{5/2}$) (Fig. 6(f)) [54]. HRTEM analysis further identified lattice fringes with a spacing of 0.321 nm, corresponding to the (111) plane of studtite ($UO_2(O_2)\cdot 4H_2O$) on the catalyst surfaces (Figs. 6(g) and 6(h), and Fig. S17 in the ESM) [55]. For ZABDC-D, this uranyl peroxide phase precipitates directly from the reaction between adsorbed UO_2^{2+} and the external H_2O_2 in solution (Eq. (9)). For systems without external H_2O_2, we propose that visible-light irradiation drives the photocatalytic generation of H_2O_2 *in situ* via oxygen reduction at the O/N-rich active sites of ZABDC. This self-generated H_2O_2 subsequently reacts with UO_2^{2+} to form studtite, analogous to the process in ZABDC-D.

$$UO_2^{2+} + H_2O_2 + 2H_2O \rightarrow (UO_2)O_2 \cdot 2H_2O(s) + 2H^+ \quad (9)$$

The UV–vis DRS showed that ZABDC exhibits a strong absorption edge across the visible light spectrum (Fig. 7(a)). The optical band gap (E_g) was determined from the Tauc plot derived from the Kubelka–Munk transformation, which is equal to 2.63 eV. Mott–Schottky analysis, performed in a standard three-electrode system, revealed a positive slope, confirming the n-type semiconductor nature of ZABDC (Fig. 7(b)). The flat-band potential was estimated from the MS plot, and the conduction band minimum (E_{CB}) was determined to be −0.41 eV. The valence band maximum (E_{VB}) was subsequently calculated using the relation $E_{VB} = E_{CB} + E_g$, yielding a value of 2.22 eV (Fig. 7(c)). The photoelectrochemical response was evaluated to probe charge carrier dynamics. ZABDC generated a stable and prompt photocurrent under visible-light illumination, indicating efficient generation and separation of photoinduced charge carriers (Fig. 7(d)). Electron paramagnetic resonance (EPR) spectroscopy was employed to identify the active species involved. As shown in Fig. 7(e), the intensity of the 2,2,6,6-Tetramethylepiperidin-1-oxyl (TEMPO) signal decreased over time, consistent with the consumption of photogenerated electrons. Control experiments with isopropanol confirmed hydroxyl radicals (·OH) are not generated in significant quantities (Fig. S18 in the ESM), allowing the TEMPO signal decay attributed to reducing electrons rather than radical quenching. These electrons are thermodynamically directed toward O_2 reduction, as the conduction band potential of ZABDC is more negative than the redox potential of $O_2/{}^{\cdot}O_2^-$ (−0.33 V vs. normal hydrogen electrode (NHE)). The consequent formation of superoxide radicals (${}^{\cdot}O_2^-$) was confirmed by time-dependent DMPO-${}^{\cdot}O_2^-$ signals, where the intensity of the peaks increases with time (Fig. 7(f)), initiating the pathway for *in situ* H_2O_2 production (Eqs. (10) and (11), and Fig. 7(c)).

Active species trapping experiments corroborated these findings (Fig. S18 in the ESM). The addition of isopropanol caused a negligible change in uranium extraction efficiency, confirming the minor role of ·OH.

In contrast, the addition of benzoquinone (${}^{\cdot}O_2^-$ scavenger) and $AgNO_3$ (electron scavenger) significantly inhibited the process. This inhibition was most pronounced in the absence of external H_2O_2, where removal efficiency dropped to 62% and 55%, respectively

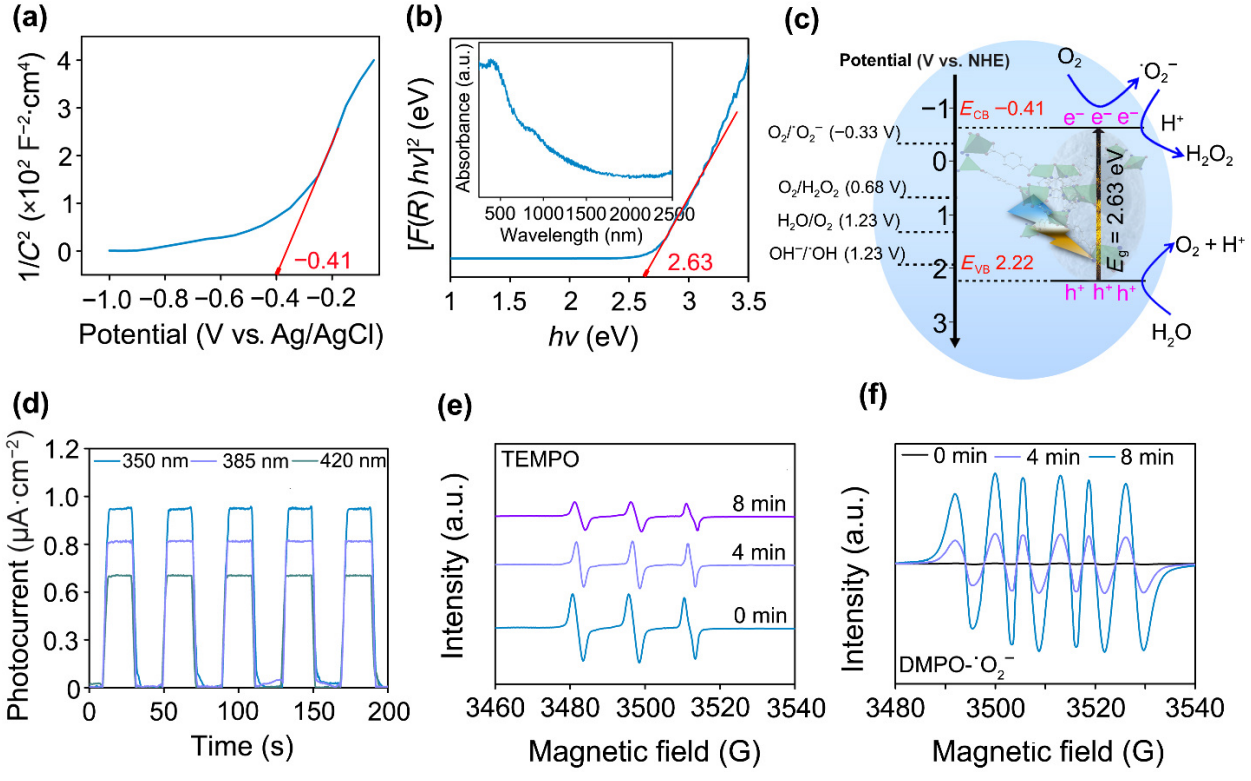

Figure 7 (a) Mott–Schottky curves. (b) Kubelka–Munk-transformed reflectance spectra, with the UV–vis diffuse reflection spectra shown in the inset. (c) Schematic illustration of the electronic band structure of ZABDC and the *in situ* generation of H_2O_2 in the ZABDC-C system. (d) Transient photocurrent density of ZABDC at different wavelengths. EPR spectra of ZABDC with (e) TEMPO and (f) DMPO-${}^{\cdot}O_2^-$.

(versus 92% and 89% with H_2O_2), demonstrating that $^{\cdot}O_2^-$ and electrons are critical for *in situ* H_2O_2 generation. The production of H_2O_2 via this pathway was independently verified by $KMnO_4$ titration. When the hole scavenger EDTA was introduced, U(VI) removal was unaffected in the presence of external H_2O_2. However, without external H_2O_2, the removal rate decreased to 68%, demonstrating that photogenerated holes (h^+) are actively consumed to facilitate the overall H_2O_2 production cycle (Eq. (11)). Taken together, these results establish a coherent photocatalytic mechanism for uranium immobilization. In the absence of external H_2O_2, photogenerated charge carriers catalyze the reduction of O_2 to $^{\cdot}O_2^-$, leading to *in situ* H_2O_2 formation. This H_2O_2 then reacts with soluble UO_2^{2+}, driving its extraction through the precipitation of insoluble uranyl-peroxide solids (Eq. (9)).

$$O_2 + e^- \rightarrow {}^{\cdot}O_2^- \quad (10)$$

$$2H^+ + e^- + {}^{\cdot}O_2^- \rightarrow H_2O_2 \quad (11)$$

4 Conclusions

In this work, we developed a facile solvothermal strategy to fabricate spherical and fluorescent Zn-adeninate-based MOF micromotors (ZABDC) through the incorporation of a short organic linker. This heuristic strategy significantly enhances micromotor stability by providing steric protection and increased hydrophobicity around the metal-linker bonds, enabling efficient autonomous propulsion in a low-concentration H_2O_2 fuel. The speed of these micromotors was further amplified under visible light illumination. The ZABDC micromotors are highly effective for the selective adsorption of radioactive UO_2^{2+} from wastewater without external agitation. Their exceptional performance can be attributed to a synergistic combination of hierarchical morphology, high surface area, pore-filling effects, abundant active sites, and self-propulsion. We elucidated a removal mechanism where photocatalytic activity and the presence of chelating sites facilitate the nucleation and growth of studtite from uranyl ions in H_2O_2. Furthermore, we demonstrated tunable and fuel-dependent collective behaviors in binary mixtures. The interactions between active ZABDC micromotors and passive colloids transitioned from predator–prey behaviors to organized schooling by altering H_2O_2 concentration. This reversible control over particle interactions, also observed with positively charged PS spheres, highlights the system's dynamic responsiveness. In summary, this work presents an "all-in-one" MOF-based micromotor platform that successfully bridges fundamental insights into active matter with a direct and efficient application in photocatalytic wastewater treatment.

Electronic Supplementary Material: Supplementary material (SEM, TEM, EDX, XRD, TGA, EXAFS, zeta potential, BET, adsorption analysis, and DFT methods) is available in the online version of this article at https://doi.org/10.26599/NR.2026.94908602.

Data availability

All data needed to support the conclusions in the paper are presented in the manuscript and the Electronic Supplementary Material. Additional data related to this paper may be requested from the corresponding author upon request.

Acknowledgements

We acknowledge the financial support from the Research Fund for International Young Scientists sponsored by the National Natural Science Foundation of China (Nos. 22150410328 and 12474195), the Research fund from Qinghai Institute of Salt lakes Chinese Academy of Sciences (No. E355HX01), the Qinghai Outstanding Youth Science Fund (No. 2025-ZJ-967J), and the Kunlun Talents High-end Innovative and Entrepreneurial Talents program of Qinghai Province (No. E540HX11). The XAFS experiments performed at KEK-PF were approved by the Program Advisory Committee (No. 2025G131) at the Institute of Materials Structure Science, KEK.

Declaration of competing interest

All the contributing authors report no conflicts of interest in this work.

Author contribution statement

M. I.: Formal analysis, funding acquisition, validation, methodology, software, writing – original draft. I. M.: Data curation, formal analysis, software. Y. Q. Z.: Funding acquisition, project administration, resources, writing – review & editing. I. M. ul H.: Formal analysis, visualization. H. K.: Validation, data curation. Y. X. G.: Project administration, funding acquisition, writing – review & editing, conceptualization, and supervision. All the authors have approved the final manuscript.

Use of AI statement

None.

References

[1] Gao, Y. X.; Xiong, Z.; Wang, J. Z.; Tang, J. Y.; Li, D. Light hybrid micro/nano-robots: From propulsion to functional signals. *Nano Res.* **2022**, *15*, 5355–5375.

[2] Yang, L.; Chen, X. X.; Wang, L.; Hu, Z. J.; Xin, C.; Hippler, M.; Zhu, W. L.; Hu, Y. L.; Li, J. W.; Wang, Y. C. et al. Targeted single-cell therapeutics with magnetic tubular micromotor by one-step exposure of structured femtosecond optical vortices. *Adv. Funct. Mater.* **2019**, *29*, 1905745.

[3] Ruiz-González, N.; Esporrín-Ubieto, D.; Kim, I.-D.; Wang, J.; Sánchez, S. Micro- and nanomotors: Engineered tools for targeted and efficient biomedicine. *ACS Nano* **2025**, *19*, 8411–8432.

[4] Urso, M.; Ussia, M.; Peng, X.; Oral, C. M.; Pumera, M. Reconfigurable self-assembly of photocatalytic magnetic microrobots for water purification. *Nat. Commun.* **2023**, *14*, 6969.

[5] Mou, F. Z.; Li, X. F.; Xie, Q.; Zhang, J. H.; Xiong, K.; Xu, L. L.; Guan, J. G. Active micromotor systems built from passive particles with biomimetic predator–prey interactions. *ACS Nano* **2020**, *14*, 406–414.

[6] Zhou, C.; Zhang, H. P.; Tang, J. Y.; Wang, W. Photochemically powered AgCl Janus micromotors as a model system to understand ionic self-diffusiophoresis. *Langmuir* **2018**, *34*, 3289–3295.

[7] Palacci, J.; Sacanna, S.; Steinberg, A. P.; Pine, D. J.; Chaikin, P. M. Living crystals of light-activated colloidal surfers. *Science* **2013**, *339*, 936–940.

[8] Huang, Y.; Lin, Z. H.; He, Q. Directional and reconfigurable assembly of active colloidal motors triggered by chemical communications. *Adv. Funct. Mater.* **2024**, *34*, 2311136.

[9] Lin, Z. H.; Si, T. Y.; Wu, Z. G.; Gao, C. Y.; Lin, X. K.; He, Q. Light-activated active colloid ribbons. *Angew. Chem., Int. Ed.* **2017**, *56*, 13517–13520.

[10] Buttinoni, I.; Bialké, J.; Kümmel, F.; Löwen, H.; Bechinger, C.; Speck, T. Dynamical clustering and phase separation in suspensions of self-propelled colloidal particles. *Phys. Rev. Lett.* **2013**, *110*, 238301.

[11] Ibele, M.; Mallouk, T. E.; Sen, A. Schooling behavior of light-powered autonomous micromotors in water. *Angew. Chem., Int. Ed.* **2009**, *48*, 3308–3312.

[12] Singh, D. P.; Choudhury, U.; Fischer, P.; Mark, A. G. Non-equilibrium assembly of light-activated colloidal mixtures. *Adv. Mater.* **2017**, *29*, 1701328.

[13] Huang, H.; Li, J.; Yuan, M. G.; Yang, H. W.; Zhao, Y.; Ying, Y. L.; Wang, S. Large-scale self-assembly of MOFs colloidosomes for bubble-propelled micromotors and stirring-free environmental remediation. *Angew. Chem., Int. Ed.* **2022**, *61*, e202211163.

[14] Zhang, X. L.; Chen, L.; Fu, L. H.; Feng, K.; Gong, J.; Qu, J. P.; Niu, R. Dual-functional metal-organic frameworks-based hydrogel micromotor for uranium detection and removal. *J. Hazard. Mater.* **2024**, *467*, 133654.

[15] Fu, L. H.; Feng, K.; Li, Q. Q.; Qin, M. T.; Yang, J.; Zhang, X. L.; Chen, L.; Gong, J.; Qu, J. P.; Niu, R. Ion-exchange induced multiple effects to promote uranium uptake from nonmarine water by micromotors. *J. Hazard. Mater.* **2024**, *480*, 136464.

[16] Zhang, J. H.; Fang, Y. M.; Lin, J. W.; Du, W. X.; Feng, Z. Y.; Lin, Y.; Xu, L. L.; Liu, L. J.; Guan, J. G.; Mou, F. Z. Generalized and scalable synthesis of manganese dioxide-based tubular micromotors for heavy metal ion removal. *ACS Nano* **2024**, *18*, 29248–29260.

[17] Ying, Y. L.; Pourrahimi, A. M.; Sofer, Z.; Matějková, S.; Pumera, M. Radioactive uranium preconcentration via self-propelled autonomous microrobots based on metal-organic frameworks. *ACS Nano* **2019**, *13*, 11477–11487.

[18] Zhang, Q. Y.; Zhang, L. J.; Zhu, J. Q.; Gong, L. L.; Huang, Z. C.; Gao, F.; Wang, J. Q.; Xie, X. Q.; Luo, F. Ultra-selective uranium separation by *in-situ* formation of π-f conjugated 2D uranium-organic framework. *Nat. Commun.* **2024**, *15*, 453.

[19] Huang, Z.-W.; Li, X.-B.; Mei, L.; Han, Y.-Z.; Song, Y.-T.; Fu, X.; Zhang, Z.-H.; Guo, Z.-J.; Zeng, J.-R.; Bian, F.-G. et al. All-in-one: Photo-responsive lanthanide-organic framework for simultaneous sensing, adsorption, and photocatalytic reduction of uranium. *Adv. Funct. Mater.* **2024**, *34*, 2404126.

[20] Yang, H. Y.; Wang, L.; Huang, X. MOF-based micro/nanomotors (MOFtors): Recent progress and challenges. *Coord. Chem. Rev.* **2023**, *495*, 215372.

[21] Tan, T. T. Y.; Cham, J. T. M.; Reithofer, M. R.; Andy Hor, T. S.; Chin, J. M. Motorized Janus metal organic framework crystals. *Chem. Commun.* **2014**, *50*, 15175–15178.

[22] Zhang, F. Y.; Li, Z. X.; Yin, L.; Zhang, Q. Z.; Askarinam, N.; Mundaca-Uribe, R.; Tehrani, F.; Karshalev, E.; Gao, W. W.; Zhang, L. F. et al. ACE2 receptor-modified algae-based microrobot for removal of SARS-CoV-2 in wastewater. *J. Am. Chem. Soc.* **2021**, *143*, 12194–12201.

[23] Jiao, L.; Wang, Y.; Jiang, H.-L.; Xu, Q. Metal-organic frameworks as platforms for catalytic applications. *Adv. Mater.* **2018**, *30*, 1703663.

[24] Hu, S. S.; Huang, J. J.; Gao, M.-L.; Lin, Z. Y.; Qian, Y. Y.; Yang, W. J.; Jiao, L.; Jiang, H.-L. Location-specific microenvironment modulation around single-atom metal sites in metal-organic frameworks for boosting catalysis. *Angew. Chem., Int. Ed.* **2025**, *64*, e202415155.

[25] Terrones, G. G.; Huang, S. P.; Rivera, M. P.; Yue, S. W.; Hernandez, A.; Kulik, H. J. Metal-organic framework stability in water and harsh environments from data-driven models trained on the diverse WS_{24} data set. *J. Am. Chem. Soc.* **2024**, *146*, 20333–20348.

[26] Wei, Y. H.; Dong, H. Y.; Wei, C.; Zhang, W.; Yan, Y. L.; Zhao, Y. S. Wavelength-tunable microlasers based on the encapsulation of organic dye in metal-organic frameworks. *Adv. Mater.* **2016**, *28*, 7424–7429.

[27] Li, T.; Kozlowski, M. T.; Doud, E. A.; Blakely, M. N.; Rosi, N. L. Stepwise ligand exchange for the preparation of a family of mesoporous MOFs. *J. Am. Chem. Soc.* **2013**, *135*, 11688–11691.

[28] Zhou, X. Y.; Li, Z. J.; Shi, Y. X.; Miao, Y. Q.; Liu, Y. Y.; Yin, R. L.; Guo, W. Q.; Qin, J. H.; Li, H. S.; Jing Li, A. et al. Piezoelectric field-modulated peroxymonosulfate nonradical oxidation of bisphenol A via Bio-MOF-1: The dominant contribution of singlet oxygen. *Chem. Eng. J.* **2024**, *492*, 152368.

[29] Mohammadzadeh, D.; Hosseini, S. A. Removal of dibenzothiophene from liquid fuels by photocatalytic desulfurization over Zn-terephthalate complex: A process modelling and optimization by response surface methodology. *ChemistrySelect* **2023**, *8*, e202302400.

[30] An, J.; Rosi, N. L. Tuning MOF CO_2 adsorption properties via cation exchange. *J. Am. Chem. Soc.* **2010**, *132*, 5578–5579.

[31] Gao, Z. H.; Xu, B. Y.; Fan, Y. Q.; Zhang, T. J.; Chen, S. W.; Yang, S.; Zhang, W. G.; Sun, X.; Wei, Y. H.; Wang, Z. F. et al. Topological-distortion-driven amorphous spherical metal-organic frameworks for high-quality single-mode microlasers. *Angew. Chem., Int. Ed.* **2021**, *60*, 6362–6366.

[32] Wei, S. J.; Ma, W. J.; Sun, M. M.; Xiang, P.; Tian, Z. Q.; Mao, L. Q.; Gao, L. Z.; Li, Y. D. Atom-pair engineering of single-atom nanozyme for boosting peroxidase-like activity. *Nat. Commun.* **2024**, *15*, 6888.

[33] Meng, K.; Zhang, J. J.; Zhu, B. C.; Jiang, C. J.; García, H.; Yu, J. G. Interfacial charge transfer in ZnO/COF S-scheme photocatalyst via Zn–N bond. *Adv. Mater.* **2025**, *37*, 2505088.

[34] Li, F.; Bu, Y. F.; Han, G.-F.; Noh, H.-J.; Kim, S.-J.; Ahmad, I.; Lu, Y. L.; Zhang, P.; Jeong, H. Y.; Fu, Z. P. et al. Identifying the structure of Zn–N_2 active sites and structural activation. *Nat. Commun.* **2019**, *10*, 2623.

[35] Yuan, B. W.; Yao, Z. H.; Qiu, C. L.; Zheng, H. Y.; Yan, Y. L.; Zhang, Q. Q.; Sun, X.; Gu, Y.; Zhong, X.; Wang, J. G. Synergistic effect of size-dependent PtZn nanoparticles and zinc single-atom sites for electrochemical ozone production in neutral media. *J. Energy Chem.* **2020**, *51*, 312–322.

[36] Liu, X. Q.; Ge, J. M.; Li, S. Y.; Yang, H. H.; Tian, H. W.; Liu, H. P.; Li, Y. X.; Zheng, X. L.; Tian, Y. P.; Cui, X. W. et al. Activating dynamic Zn–ZnO interface with controllable oxygen vacancy in CO_2 electroreduction for boosting CO production. *Green Chem.* **2025**, *27*, 6133–6144.

[37] Sutton, J.; Grause, G.; Rida Hmayed, A. A.; Street, S. T. G.; Dove, A. P.; Wood, J. Organocatalytic glycolysis of polyethylene terephthalate and product separation by membrane filtration. *Chem. Eng. J.* **2025**, *512*, 162400.

[38] Fiala, R.; Sklenář, V. ^{13}C-detected NMR experiments for measuring chemical shifts and coupling constants in nucleic acid bases. *J. Biomol. NMR* **2007**, *39*, 153–163.

[39] Liu, C.; Li, T.; Rosi, N. L. Strain-promoted "click" modification of a mesoporous metal-organic framework. *J. Am. Chem. Soc.* **2012**, *134*, 18886–18888.

[40] Wang, J.-X.; Yin, J.; Shekhah, O.; Bakr, O. M.; Eddaoudi, M.; Mohammed, O. F. Energy transfer in metal-organic frameworks for fluorescence sensing. *ACS Appl. Mater. Interfaces* **2022**, *14*, 9970–9986.

[41] Kochergin, Y. S.; Villa, K.; Nemeškalová, A.; Kuchař, M.; Pumera, M. Hybrid inorganic–organic visible-light-driven microrobots based on donor–acceptor organic polymer for degradation of toxic psychoactive substances. *ACS Nano* **2021**, *15*, 18458–18468.

[42] Liu, X. X.; Sun, X.; Peng, Y. X.; Wang, Y.; Xu, D. D.; Chen, W. J.; Wang, W.; Yan, X. H.; Ma, X. Intrinsic properties enabled metal organic framework micromotors for highly efficient self-propulsion and enhanced antibacterial therapy. *ACS Nano* **2022**, *16*, 14666–14678.

[43] Ikram, M.; Peng, G. G.; Hassan, Q. U.; Basharat, M.; Li, Y. R.; Zeb, S.; Gao, Y. X. Photoactive and intrinsically fuel sensing metal-organic framework motors for tailoring collective behaviors of active-passive colloids. *Small* **2023**, *19*, 2301625.
[44] Chang, X. C.; Chen, C. R.; Li, J. X.; Lu, X. L.; Liang, Y. Y.; Zhou, D. K.; Wang, H. C.; Zhang, G. Y.; Li, T. L.; Wang, J. et al. Motile micropump based on synthetic micromotors for dynamic micropatterning. *ACS Appl. Mater. Interfaces* **2019**, *11*, 28507–28514.
[45] Mei, D. C.; Liu, L. J.; Yan, B. Adsorption of uranium(VI) by metal-organic frameworks and covalent-organic frameworks from water. *Coord. Chem. Rev.* **2023**, *475*, 214917.
[46] Pan, J. M.; Xiao, B. T.; Zhu, W.; Yang, Y. N.; Huang, H. L.; Lian, Z. C.; Zhang, T.; Qiu, F. X.; Xue, S. L.; Pang, H. Photocatalytic uranium extraction boosted by dual effective active sites of porphyrin metal-organic frameworks. *Nano Res.* **2024**, *17*, 6713–6720.
[47] Chen, L.; Fu, L. H.; Feng, K.; Zhang, X. L.; Gong, J.; Qu, J. P.; Niu, R. Ion exchange-based microreactors harness self-generated pH gradients and long-range flow for dual-enhanced uranium extraction. *Adv. Funct. Mater.* **2025**, *35*, e09597.
[48] Pan, Z. Z.; Bártová, B.; LaGrange, T.; Butorin, S. M.; Hyatt, N. C.; Stennett, M. C.; Kvashnina, K. O.; Bernier-Latmani, R. Nanoscale mechanism of UO_2 formation through uranium reduction by magnetite. *Nat. Commun.* **2020**, *11*, 4001.
[49] Xiong, X. H.; Yu, Z. W.; Gong, L. L.; Tao, Y.; Gao, Z.; Wang, L.; Yin, W. H.; Yang, L. X.; Luo, F. Ammoniating covalent organic framework (COF) for high-performance and selective extraction of toxic and radioactive uranium ions. *Adv. Sci.* **2019**, *6*, 1900547.
[50] World Health Organization. *Guidelines for Drinking-Water Quality: Fourth Edition Incorporating the First and Second Addenda*; World Health Organization: Geneva, 2022.
[51] Liu, R.; Wang, Z.-Q.; Liu, Q.-Y.; Luo, F.; Wang, Y.-L. A zinc MOF with carboxylate oxygen-functionalized pore channels for uranium(VI) sorption. *Eur. J. Inorg. Chem.* **2019**, *2019*, 735–739.
[52] An, J.; Geib, S. J.; Rosi, N. L. Cation-triggered drug release from a porous zinc-adeninate metal-organic framework. *J. Am. Chem. Soc.* **2009**, *131*, 8376–8377.
[53] Song, Y. C.; Ma, X.; Tan, H. H.; Liu, Z.; Liu, C. T.; Shen, C. Y.; Yang, P. P.; Li, S. W. Hollow Zn/Co zeolitic imidazolate framework-implanted composite hydrogel for highly efficient uranium extraction from seawater. *Nano Res.* **2023**, *16*, 10451–10461.
[54] Wang, X.; Xu, W.; Cui, W.-R. Modulating conjugated microporous polymers via cyclization as a remarkable photo-enhanced uranium recovery platform. *J. Hazard. Mater.* **2024**, *463*, 132846.
[55] Fu, H.; Pan, Y. H.; Cai, Z. Y.; Deng, Y. X.; Hou, M. C.; Wei, Y. Z.; Fujita, T.; Ning, S. Y.; Wang, Y. B.; Zhang, S. L. et al. Bi_2O_3/g-C_3N_4 hollow core–shell Z-scheme heterojunction for photocatalytic uranium extraction. *Nano Res.* **2024**, *17*, 5845–5855.